Assessment of swashplateless rotor systems for sensor carrying drones

An investigation into control, efficiency, and feasibility

Master's thesis in Mobility Engineering
Master's thesis in Information and Communication Technology

Jesper Nordling
Simon Björklund

DEPARTMENT OF MECHANICS AND MARITIME SCIENCES
CHALMERS UNIVERSITY OF TECHNOLOGY
Gothenburg, Sweden 2025
www.chalmers.se

Master's Thesis in Mechanics and Maritime Sciences

Assessment of swashplateless rotor systems for sensor carrying drones

An investigation into control, efficiency, and feasibility

Jesper Nordling
Simon Björklund

CHALMERS
UNIVERSITY OF TECHNOLOGY

Department of Mechanics and Maritime Sciences
Chalmers University of Technology
Gothenburg, Sweden 2025

Assessment of swashplateless rotor systems for sensor carrying drones
An investigation into control, efficiency, and feasibility
Jesper Nordling
Simon Björklund

Supervisor: Tarun Kadri Sathiyan, Department of Mechanics and Maritime Sciences
Examiner: Ola Benderius, Department of Mechanics and Maritime Sciences

Master's Thesis 2025
Department of Mechanics and Maritime Sciences
Chalmers University of Technology
SE-412 96 Gothenburg
Sweden
Telephone +46 31 772 1000

Cover: Teetering vs dual hinge rotor

Gothenburg, Sweden 2025

Assessment of swashplateless rotor systems for sensor carrying drones
An investigation into control, efficiency, and feasibility
Jesper Nordling
Simon Björklund
Department of Mechanics and Maritime Sciences
Division of Vehicle Engineering and Autonomous Systems
Chalmers University of Technology

Abstract

This thesis investigates two rotorhead configurations, a fully articulated dual hinge and a semi-rigid teetering hinge rotor, for potential use in swashplateless helicopters or drones, aiming to expand the understanding of their respective mechanical and aerodynamical behaviours. Experiments were conducted on a fixed test rig designed for easy interchangeability between the two rotor types. Both rotors were tested with identical blades at fixed pitch angles of 8°, 10°, and 12°, using the same control system.

Three test types were performed. First, a constant roll input was applied while rotor speed varied from 500 to 3000 RPM, across three increasing roll magnitudes. Second, a step response test measured the time required for the rotor to transition from maximum to minimum roll output, assessing dynamic response. Third, a roll sweep test was conducted at approximately 2500 RPM using stepwise increases in roll input. High-speed video analysis was used to observe dynamic behaviour.

Results show that the fully articulated dual hinge rotor provides more effective thrust vectoring across all roll inputs and RPMs, while operating at significantly lower vibration levels. Both rotors exhibited similar energy consumption and roll rates. While the dual hinge rotor's improved thrust control and smoother operation suggest advantages for general purpose drones and helicopters, especially those carrying sensitive sensors and equipment, the semi-rigid teetering hinge rotor's simplicity and robustness is attractive for applications where mechanical reliability, weight reduction, and ease of maintenance are prioritized. Further exploration of teetering rotor concepts, especially in alternative configurations and with a further optimized control system, may reveal additional potential not fully captured in this study.

Keywords: UAV, drone, swashplateless, cyclic control, swashplate, dual hinge, teethering, semi-rigid, fully-actuated, PX4

Preface

This report presents the outcome of our master's thesis project carried out at the Department of Mechanics and Maritime Sciences at Chalmers University of Technology during the spring of 2025.

Acknowledgements

We would like to thank our supervisor, Ola Benderius, for his support throughout this project. We are also especially grateful to Isak Jonsson and Professor Valery Chernoray for granting us access to the laboratory facilities, supplying the equipment necessary to build and set up the test rig and providing valuable feedback and ideas along the way. We also thank the Department of Mechanics and Maritime Sciences for providing funding that made this work possible.

Jesper Nordling, Simon Björklund, Gothenburg, June 2025

List of Acronyms

Below is the list of acronyms that have been used throughout this thesis listed in alphabetical order:

BEC	Battery Eliminator Circuit
BLDC	Brushless Direct Current
CoG	Centre of gravity
ESC	Electronic Speed Controller
PCB	Printed Circuit Board
RC	Radio-Controlled
RPM	Revolutions per minute
SPI	Serial Peripheral Interface
ADC	Analog-Digital Converter
AoA	Angle of Attack
BEMF	Back- electro magnetic field

Nomenclature

Below is the nomenclature of indices, sets, parameters, and variables that have been used throughout this thesis.

Parameters

F_z	Vertical thrust [N]
F_x	Horizontal thrust [N]
F_{res}	Resultant thrust [N]
ϕ_1	Flap hinge rotation
ϕ_2	Lag pitch hinge rotation
θ	Lag pitch hinge angle
θ_m	Motor position

Variables

$\theta_{actuation}$	Actuation phase
$A_{actuation}$	Actuation amplitude
T	Modulation actuation signal
T_{coll}	Collective Control signal
T_{sp}	Total actuation setpoint

Contents

List of Figures

List of Tables

1

Introduction

Unmanned aerial vehicles (UAVs) are increasingly used in applications such as search and rescue, public safety, infrastructure inspection, and package delivery. Many of these applications rely on onboard sensors, e.g., high-resolution cameras, LiDAR, and spectrometers which are often sensitive to vibrations and rapid movements. Multirotor drones, particularly quadcopters, are widely used due to their simple construction and ease of control. However, their small propellers limit efficiency, and they often require expensive and heavy stabilization systems to ensure smooth data collection. Larger multirotor configurations (e.g., octocopters) can improve stability but at the cost of reduced range and efficiency.

Fixed-wing drones offer significantly higher aerodynamic efficiency but lack the ability to hover or maneuver in confined spaces. Hybrid solutions, such as vertical take-off and landing (VTOL) drones, combine both flight modes but introduce additional complexity and weight penalties.

Helicopters, equipped with a main rotor and a tail rotor, achieve higher efficiency in forward flight and smoother flight dynamics due to their larger rotor blades and ability to control pitch and roll without tilting the entire aircraft. This is typically achieved using a swashplate mechanism, as shown in Fig. 1.1. However, swashplate systems are mechanically complex, requiring precise calibration and frequent maintenance.

In 2013, a successful swashplateless rotor was developed, eliminating the complex mechanics of a traditional helicopter while preserving its desired flight characteristics. Research has since continued, leading to the development of more refined rotor types, the two most recent being a semi-rigid design (hereby denoted as the teethering hinge) and a fully articulated design (dual hinge). Despite these advancements, a comprehensive comparison between these two swashplateless rotor designs remains, leaving questions regarding their relative performance unanswered.

This thesis aims to investigate their performance in terms of control effectiveness, mechanical complexity, and key performance metrics such as efficiency and power consumption across a wide range of flight envelopes to bridge this knowledge gap.

1.1 Background

The first successful attempt at a swashplateless rotor featured a rigid central hub with two lag-pitch hinges [1]. While the hub design was simple, it introduced vibrations due to the lack of a flapping hinge, which is present in semi-rigid and fully articulated rotor systems.

A few years later, this work was followed by the introduction of a dual-hinge rotor type [2]. This rotor, in addition to using lag-pitch hinges, incorporated two flapping hinges, allowing the blades to flap freely instead of bending as in the rigid version. The new rotor type successfully reduced vibrations compared to the earlier design and provided a smoother, more predictable response. To achieve cyclic blade pitch control without a swashplate or blade pitch actuators, a dynamic model was implemented where torque modulation of the motors forced the blades to pitch according to control commands. A flapping hinge was also introduced to reduce bending moments in the blades and minimize airframe vibrations [2], resulting in a smooth, harmonic flapping response. The system achieved a total blade deflection of 14°.

In pursuit of further simplicity, an alternative approach was explored where the rotor flapping hinges was replaced by one central teethering hinge [3]. By utilizing two symmetrical actuators in a coaxial configuration, a coaxial helicopter was created without a swashplate or blade pitch actuators. The two actuators generated cyclic response through torque modulation, enabling thrust vectoring and full six-degree-of-freedom control. Through thrust vector control, the MAV could independently control body moments, making it possible to hover in non-upright orientations and accelerate without tilting.

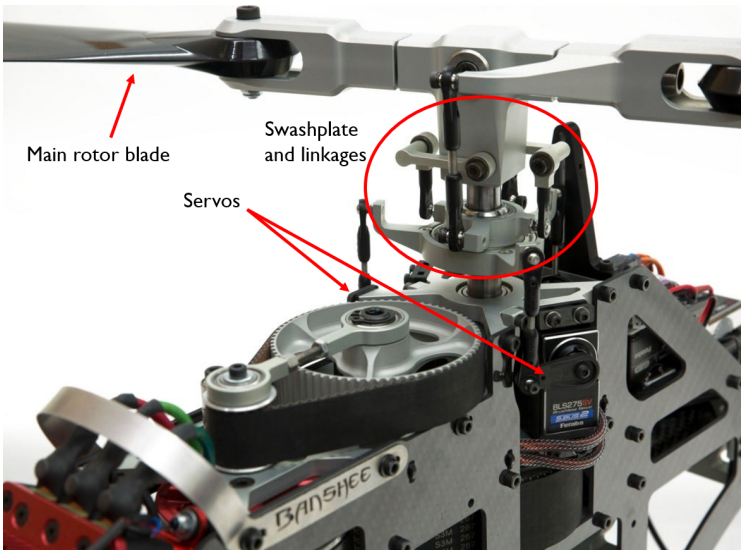

Figure 1.1: Swashplate of small RC helicopter.

1.2 Research questions

The goal of this thesis was to implement an RPM-modulated motor control system for cyclic control of a single-rotor setup and to design and construct the required rotor mechanism. A motor and rotor head was mounted on a test rig equipped with load cells to measure thrust and torque generated under cyclic control. Based on this system, the thesis addressed the following research questions:

- **Q1:** How do the two swashplateless rotor designs compare in terms of manoeuvrability, stability, and control effectiveness for sensor applications?
- **Q2:** How does the cyclic control achieved through RPM modulation differ between the two designs in terms of energy efficiency, power consumption, and aerodynamic performance?
- **Q3:** What are the trade-offs between the two designs in terms of mechanical complexity and dynamic behaviour relevant to sensor carrying drone applications?

1.3 Limitations

The study is subject to the following constraints:

- **Scope:** The study focuses on comparing two specific swashplateless rotor configurations. Other possible variations or hybrid control mechanisms were outside the scope of this research.
- **System implementation:** The analysis focuses on functional proof of concept implementations rather than fully optimized or production-ready designs to give both rotors the same operational constraints.
- **Prototype development:** A flying prototype is not guaranteed and depends on time constraints. Priority will be given to data collection from the rotor test rig.

2
Theory

To understand the advantages and challenges of swashplateless rotor designs, it is essential to review their underlying principles, historical development, and key performance factors. This chapter outlines the fundamental concepts of rotor dynamics, the evolution of swashplateless control methods, and their implications for possible UAV applications.

2.1 Swashplateless rotors

Traditional helicopters rely on a swashplate to control the cyclic and collective pitch of the rotor blades. While effective, swashplate mechanisms introduce mechanical complexity, require precise calibration, and increase maintenance demands. An alternative approach to rotor control was introduced by Paulos and Yim in 2013 [1], replacing the swashplate with a mechanism based on motor torque modulation. This invention eliminated the need for pitch linkages by using high-frequency variations in motor torque to induce cyclic blade pitch changes in combination with angled *lag-pitch hinges*.

2.1.1 Evolution of swashplateless rotors

The first swashplateless rotor system utilized a rigid central hub with separate *lag-pitch hinges* [1]. This allowed the rotor hub to create the lag pitch actuation through torque modulation as seen in Fig. 2.1. The torque modulation causes an acceleration and retardation of the blades. By utilizing inertia of the blades they naturally swing back during the acceleration thanks to the free moving hinge. Since the hinge is positioned at an angle the blade is also forced to pitch, increasing the angle of attack (AoA). On the opposite side of the hub where the second blade is attached, the lag-pitch hinge instead forces the blade to pitch less reducing the AoA.

By carefully controlling the acceleration and retardation of the blades the AoA can be controlled as it rotates. The resulting lift generated by each blade depends on the AoA and since an asymmetry has been introduced a difference force is generated on each side resulting in a torque moment around the axis of modulation. This results in the hub acting very similar to a real swashplate on a conventional helicopter which allows for cyclic control. In Fig. 2.1, the first panel illustrates the blade increasing its AoA during the acceleration phase, the second panel showing the stop in acceleration and start of of the deceleration phase followed by the third

panel showing the decrease in AoA.

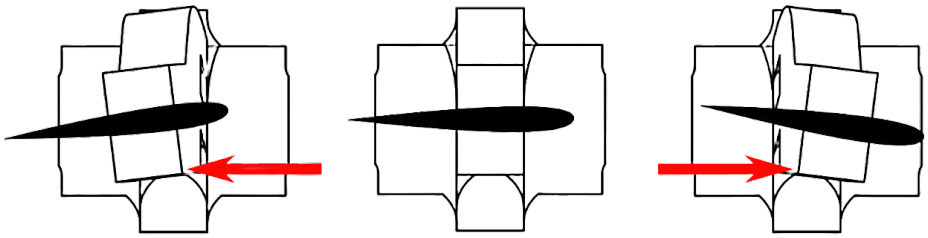

Figure 2.1: Lag pitch hinge dynamics under acceleration.

The rigid rotor hub, although simple in construction, has an inherent drawback. As lift is generated, the constantly varying aerodynamic forces on the blades produce equal and opposite reactions. Since the blades are rigidly attached and cannot move freely to relieve these loads, they bend instead. This elastic deformation introduces additional stresses in the blades and transmits vibrations to the hub [2]. Such limitations motivated the development of more advanced rotor configurations.

- **Dual hinge rotor:** To address the vibration problem, a *dual hinge* design was introduced [2]. This configuration incorporated both lag-pitch hinges and flap hinges, allowing the blades to flap freely rather than flexing under aerodynamic loads. The dual-hinge system significantly improved stability by reducing bending moments and providing a smoother flight response. A schematic drawing of it can be found in Fig. 2.2.

- **Teetering hinge rotor:** Seeking further mechanical simplification, a *teetering-hinge* configuration was later developed [3]. This system replaced individual blade flap hinges with a single central hinge, reducing part count and maintenance requirements. By using two actuators in a coaxial arrangement, cyclic control was maintained without a swashplate or blade pitch actuators, allowing efficient thrust vectoring and enabling non-traditional flight orientations.

Comparison and research focus

Both rotor designs present unique advantages and trade-offs. The dual-hinge system enhances stability and control but retains a more complex mechanical structure. In contrast, the teetering-hinge design simplifies construction while relying more on dynamic control inputs. This study will evaluate these two rotor types, focusing on their suitability for UAV applications involving sensor payloads. Key performance metrics such as manoeuvrability, stability, power and mechanical complexity will be assessed through experimental testing.

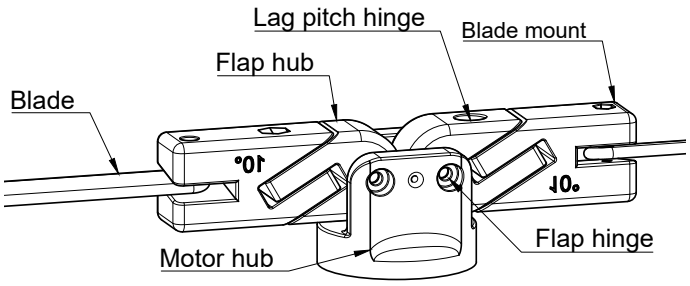

Figure 2.2: Parts of a fully articulated rotor (dual hinge).

2.2 Autopilot

The brains of the operations in the microcontroller is the PX4 flight stack [5]. The flight stack takes control commands either from a hand controller or a navigation commander depending on flight mode such as assisted stable flight, acrobatics, positional or waypoint based. The control commands feeds through the PID-chain according to Fig. 2.3. This creates thrust and angular rate setpoints which mixer block diagram interpret and converts to actuator commands such as motors and servos on the vehicle.

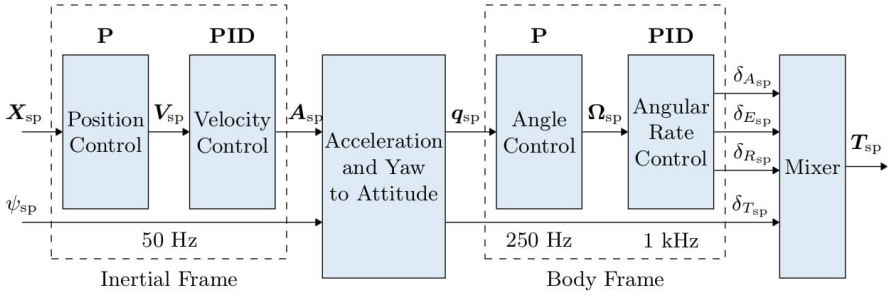

Figure 2.3: Multicopter control architecture [5]

2.3 Aerodynamics of rotors

In this thesis two traditional off-the-shelves radio-controlled (RC) helicopter rotor blades are utilized as the lift generator. The airfoil shape of the blades allows it to create lift by moving through the air as described by Eq. 2.1.

$$L = \frac{1}{2}\rho v^2 S C_L \tag{2.1}$$

where ρ is the air density, v is the airspeed, S is the relevant surface area and C_L is the lift coefficient of the airfoil [6]. Therefore, as the airfoil moves faster through air the lift increases by square of the airspeed $L \propto v^2$. Longer blades experiences higher flow speed further out from the centre point of the rotational axis according to $v = \omega r$ where ω is the rotational speed in radians per second and r is the radius at

the specific area where the lift is being calculated. So the maximum lift is generated at the outer most part of propeller until it reaches the tip vortices [7].
The lift generated can also be calculated using Eq. 2.2 [9].

$$L = \rho n^2 D^4 C_L \tag{2.2}$$

where n is the rotational speed of propeller in revolutions per second (RPM) and D is diameter. The power required to drive it can also be calculated as well using Eq. 2.3 [9]

$$P = \rho n^3 D^5 C_P \tag{2.3}$$

The coefficient of lift and power (C_P) depends partially on the AoA of the blade and the camber and chord line ratio. If the camber equals the chord line the airfoil is symmetrical and the C_L is zero at zero AoA [8]. As the AoA increases the C_L increase which increases the generated lift.

2.4 Swashplateless control principles

To actuate the blades (change pitch), the motor is accelerated, creating an opposing force $F_\phi = m_{prop}a$ as seen in the hub reference frame as seen in Fig. 2.6. This forces the blade backwards allowed by the lag pitch hinge, and since the lag pitch hinge is angled by $\theta = 30°$ the rotation ϕ_2 forces the blade to pitch increasing/decreasing the AoA depending on sign of the value θ.

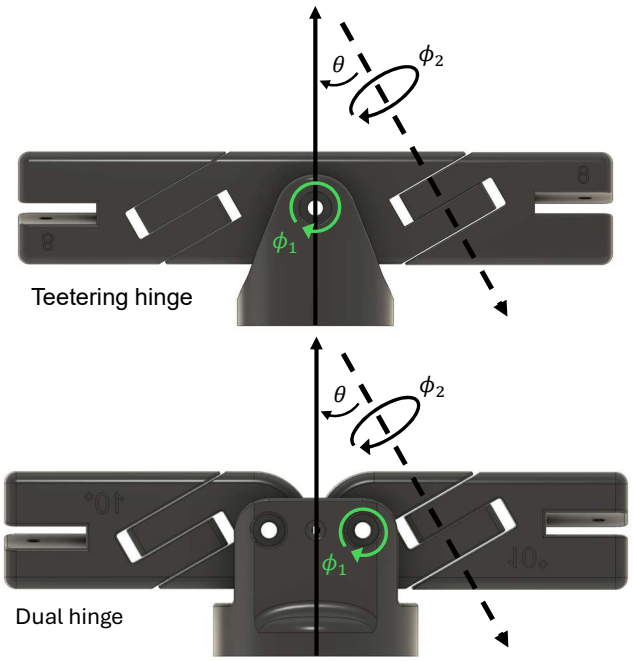

Figure 2.4: Flap and lag pitch hinge kinematics.

By periodically modulating the requested motor speed in sync with the rotation of motor the acceleration can be carefully controlled as seen in Fig. 2.5. By increasing

the maximum acceleration the resulting AoA increases. To create smooth modulation a pure sine wave is used for controlling the acceleration of the motor where the argument equals to the sum of the current motor position angle θ_m and current direction actuation phase θ_a as seen in Eq. 2.6. The actuation phase is calculated by the arctangent of the ratio between the current roll and pitch set-point requested by the flight controller seen in Fig. 2.3 using Eq. 2.4.

An amplification factor A_a scales the cosine depending on the magnitude of roll and pitch set-point calculated using Eq. 2.5.

$$\theta_a = \arctan\left(\frac{y_\Omega}{x_\Omega}\right) \tag{2.4}$$

$$A_a = \sqrt{x_\Omega^2 + y_\Omega^2} \tag{2.5}$$

$$T = A_a \cos(\theta_m + \theta_a) \tag{2.6}$$

$$T_{sp} = T + T_{coll} \tag{2.7}$$

The resulting movement for a full rotation can be seen in Fig. 2.5. Between zero and 180° the motor accelerates, but maximum acceleration is achieved between 0-90°. One blade therefore reaches its max AoA at the 90° position, but importantly does not produce maximum lift due to a complex phenomenon known as aerodynamic phase lag. Maximum lift is actually generated at the 180° position, just before the motor starts decelerating. When decelerating, the AoA gradually decreases before reaching minimum AoA at 270° and max negative lift at 0°.

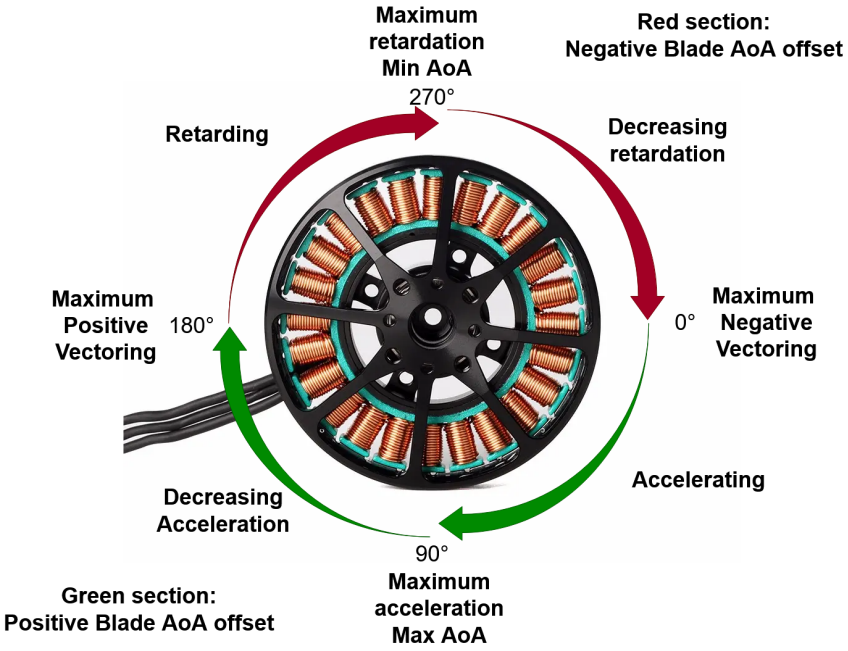

Figure 2.5: Motor action for a full modulation cycle.

The result of this modulation allows for the cyclic thrust to be created, with more lift being generated on the on left side compared to the right due to the opposing

lag-pitch hinges. Fig. 2.6 highlights how the motor acceleration increases the blade pitch on one side and consequently decreases on the opposing side, enabling thrust vectoring. The resulting roll direction depends on where during the rotation the motor is commanded to accelerate/decelerate.

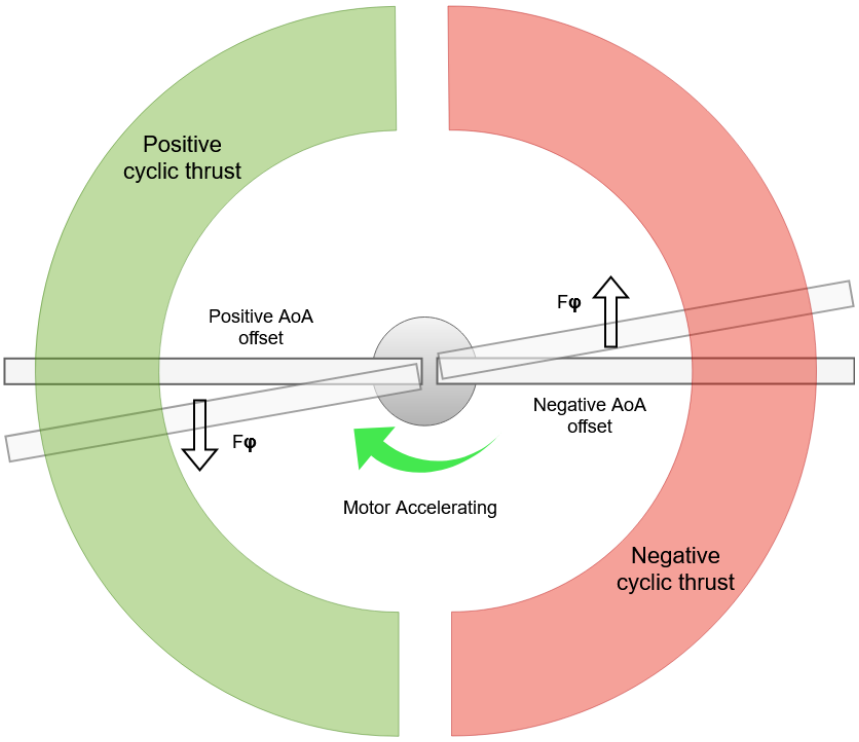

Figure 2.6: Blade movement during roll.

3
Method

This chapter describes the methods used to design, build, and test the rotors evaluated in this thesis. The work combined careful mechanical design, development of a solid experimental setup, and systematic data processing to ensure that meaningful and repeatable measurements could be obtained from the experiments. Particular attention was given to ensure fair comparisons between the rotors and to isolate the key performance characteristics of interest.

3.1 Design and manufacturing

One of the fundamental aspects of this thesis was to scale up the rotor size, which introduced several new design considerations. The primary design requirements were: (1) minimal weight difference between the rotors, (2) same blade mounting solution and blade diameter, (3) same articulation freedom and kinematics in all hinges (with endstops) and (4) sufficient structural strength for the increased loads. A key limitation was that the rotor needed to be 3D printed, primarily to enable rapid production and reduce cost, but also to allow for easy design revisions. The parts were printed in PETG, chosen for its low cost, printability, and strength.

To ensure that both rotors operated under comparable conditions, specifically similar weight, rotor diameter, and articulation freedom, each flap and motor hub had to be precisely designed without compromising structural integrity. The first iteration featured a design similar to the dual-hinge concept presented earlier [2], but was revised using larger screws and nylon locking nuts instead of thin steel pins, due to the significantly larger blade diameter and increased loads exerted on this rotor.

This design was later updated with more uniform blade grips to better match the flap hubs, maintain the blade's CoG closer to the rotor's plane of rotation, and simplify assembly and alignment. Fig. 3.1 illustrates the design evolution from the initial hinge configuration to the final integrated flap hub and blade grip.

Since the blades were sourced from a known RC helicopter, their operational specifications could be estimated. A maximum RPM of 3500 was determined to cover most flight envelopes, and the rotor hub was therefore FEM-analysed at 5000 RPM to provide an adequate safety margin. The analysis focused on stress concentrations around the lag pitch hinge and flap hinge under centrifugal loading. The results indicated acceptable safety factors for yield strength.

The lag-pitch hinge angle was set to 30°. Firstly, it allows for a relatively short and compact blade mount, as a lower angle directs more of the motion radially compared to a steeper hinge. Secondly, results from a previously built swashplate-less helicopter [11] indicated that a lower hinge angle required less control input for the same mechanical output. The potential trade-off is that a lower angle may lead to a less stable rotor, which could demand more precise tuning of the control system.

In Figs. 3.2 and 3.3 exploded views can be found of both rotors.

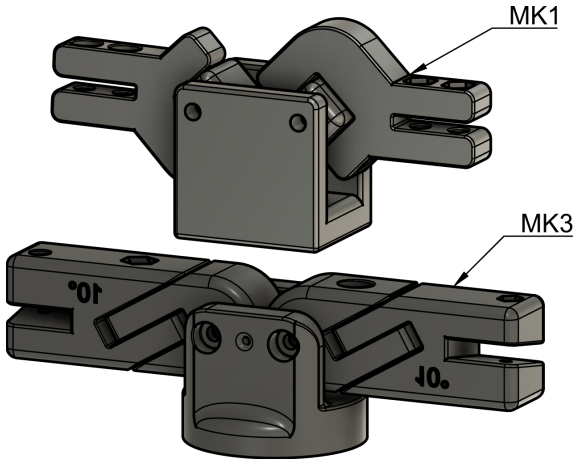

Figure 3.1: Dual hinge MK1 and MK3.

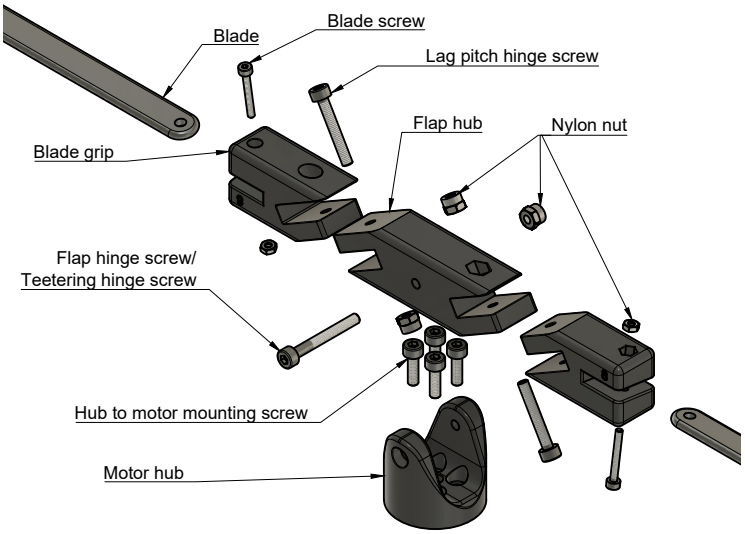

Figure 3.2: Exploded view — teetering hinge.

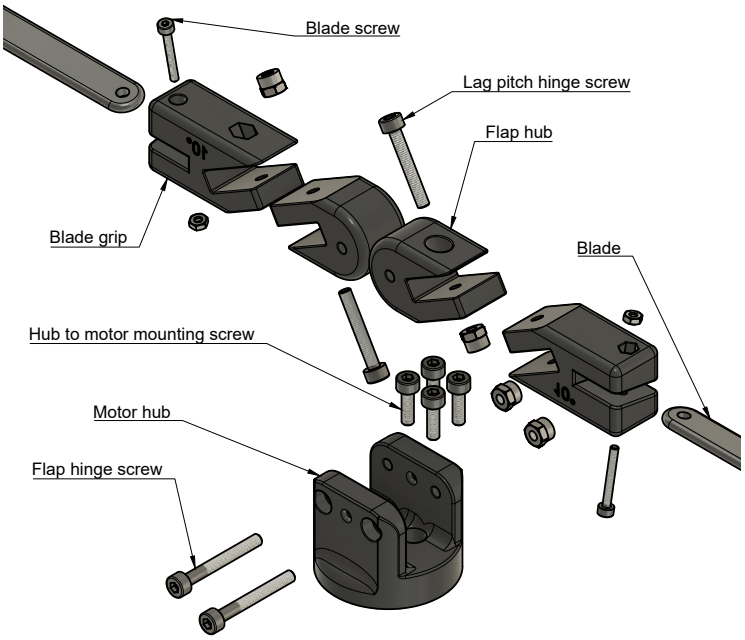

Figure 3.3: Exploded view — dual hinge.

3.2 Experimental setup

To safely and accurately test the different rotor types, a test rig was built, allowing for controlled experimentation and data collection under various flight conditions.

3.2.1 Hardware

The experimental setup was built from aluminium profiles with a baseplate on which the loadcells were mounted in horizontally with the rotor mounted in the middle. A detailed outline of the setup can be found in Fig. 3.4 of a rotor test rig designed to measure thrust, torque, and cyclic response of a swashplateless rotor system. Key components are listed in Table 3.1.

Table 3.1: Overview of experimental hardware

Component	Description
Motor	T-motor MN6007 II 160KV
Rotor blades	HD230AT from the Align T-Rex 300X
Load cell	2x 5 kg
Amplifier/ADC	HX711
ESC	Flycolour X-Cross HV3 PRO 80A
Flight controller	Pixhawk 6X-RT

At the bottom, a base plate was used for mounting the load cells. On top of this, a custom printed circuit board (PCB) with a thermistor and a magnetic encoder (Hall effect sensor) was mounted. Above this, the motor was installed, with a diametrically magnetised magnet mounted on the main shaft. This setup enabled the Hall effect sensor to read the exact position of the motor, necessary for torque modulation.

The Arduino UNO runs an infinitely looping software which reads out data from the loadcell amplifier over a simplified SPI-protocol. The load cell amplifier contains a 24-bit ADC (analog-digital converter) converting the voltage value from the load cell to a digital binary value. The data from both amplifiers read out at the same time and transmitted to the Pixhawk flight controller over a UART serial interface. The Pixhawk timestamps the data and the saves in the same log file as all of our other data removing any time ambiguity in the data and synchronising measurements.

The encoder PCB uses the Hall effect magnetic encoder AEAT-9955 with 18 bits of angular resolution. The highest update rate reached from it was 1 kHz allowing angular rate controller described in Fig. 2.3 to run at full speed with updated motor position data for each iteration and at 3000 rpm this resulted in 20 position updates per revolution.

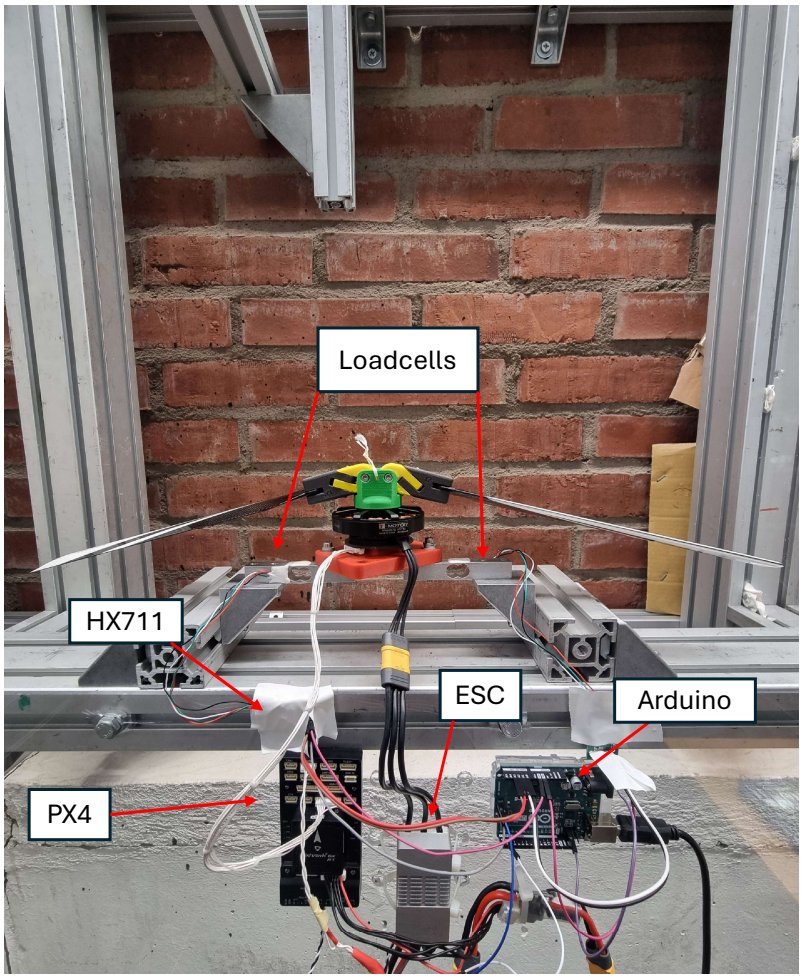

Figure 3.4: Test setup.

3.2.2 Sensor calibration

To remove the starting value offset provided by the amplifier and the loadcells an offset measurement is done to determine the baseline. On power-on the Arduino measures 100 samples from both loadcells and determines the offset effectively zeroing any coming measurments.

The loadcells were calibrated by attaching a string to the rotor hub. The string passed through a pulley mounted so that the string achieved an angle of 70° to the horizontal plane. This enabled calibration of both X and Y (horizontal and vertical) thrust in the same test. At the other end weights of 0–2.7 kg were attached in 200g increments. The corresponding force readings were recorded and a linear curve fit was performed to finalize the calibration process for both the X and Y axis. The calibrated load cell signals were converted to physical force measurements using the following relationships: the vertical force component was calculated as $F_z = |\text{loadcell}_1 + \text{loadcell}_2|$, and the horizontal force component as $F_x = |\text{loadcell}_1 - \text{loadcell}_2|$.

3.2.3 Software

For controlling the motor and ESC, a flight controller capable of handling the required bandwidth had to be used. The software was the open-source PX4 firmware [4], which incorporated an autopilot into the flight controller, making the transition from a test rig to a flight-ready helicopter easier.

To start, the base helicopter library was used since it included all the standard flight commands and actuations of a conventional helicopter. The base code was then modified to take inputs from the magnetic encoder and translate them into motor commands to achieve the requested flight control.

Two custom applications were developed within the PX4 software for this project. The first was a driver that initialized the AEAT9955 sensor and read data from the magnetic encoder. The second was a custom actuation effectiveness mixer, which converted rate setpoints into motor actuation commands.

When applications in the PX4 software stack share data, they published the data onto a publish/subscribe model called uORB topics. These topics were logged in real-time and saved onto an SD card mounted on the flight controller. This setup allowed for recording data such as power draw, motor speeds, and motor actuation.

The control strategy relied on RPM modulation to achieve cyclic blade control. The motor control software implemented the following logic:

Algorithm 1 Cyclic control algorithm

```
while experiment_running do
    read_sensor_data()
    compute_control_command()
    adjust_motor_RPM(control_signal)
    log_data()
end while
```

3.2.4 Experimental design and execution

To evaluate the performance of the two swashplateless rotor designs, a series of preprogrammed scripts were run in the flight controller to enable repetitive testing with identical inputs across all rotor configurations. Calibrations of the loadcells were made every new day and after a rotor change.

1. **RPM sweep at fixed roll commands**
   The roll command was fixed at 25%, 50%, and 75%, while the RPM was varied from approximately 750 to 3000.
   Tests were conducted for each rotor and all blade angle configurations.
   Purpose: To analyse how RPM affects thrust distribution in the X and Z directions.

2. **Roll command sweep at constant RPM**
   The RPM was held constant at approximately 1900, while the roll command was varied from 0% to 100%.
   Purpose: To evaluate stability and thrust performance under varying control inputs at medium to high RPM.

3. **Transient step response test**
   A fixed roll command at a fixed RPM was applied in one direction, followed by an immediate switch to the opposite roll command. The time it took for the rotor to produce equivalent thrust in the opposite direction was recorded. The step response is measured by calculating the rise time from 10% to 90% of minimum and maximum value during the transient step response. The resulting rise time is difference in time between these two ADC values.
   Purpose: To evaluate the response time and dynamic stability of the rotor.

4. **Slow-motion filming**
   Various scripts combining roll commands and RPMs at different camera angles were executed.
   Purpose: To visually assess rotor dynamics.

3.3 Post processing

After each test run, data were logged by the flight controller and exported as a ULog log file containing data from all the logged data topics. These files were parsed using the open-source software PlotJuggler [12], which enabled quick and efficient visualisation of all run parameters and provided a fast way to transform millions of data points. The relevant parameters were then exported as CSV files and further processed using `pandas` in Python.

3.3.1 Data manipulation and filtering

Processing began by importing the raw measurement data from CSV files using `pandas`, a Python library for efficient data manipulation and analysis, selecting only relevant sensor channels to reduce memory usage and processing time. Initial cleaning included aligning timestamps such that all time series began at zero. Linear interpolation was applied to fill missing values, caused primarily by differing sensor sampling rates.

Outliers were removed using the interquartile range (IQR) method with a threshold of 1.5×IQR. Outliers were replaced with NaNs and subsequently interpolated linearly to maintain signal continuity without introducing step changes. This procedure was applied after unit conversion and load cell calibration.

Since the RPM sweep and roll sweep tests were executed through predefined scripts, average values were extracted around known target timestamps to generate point-based summaries of force and power at specific RPM and roll levels. An example of this is shown in Fig. 3.5, where each "level" corresponds to a predefined RPM step in the range 750–3000 RPM.

Due to undersampled and noisy timeseries of the voltage and current data, additional processing was required to obtain more useful power data. Cumulative energy draw (in joules) was calculated by integrating the power curve over time using the trapezoidal method. After applying the same point selection approach used for force data, the energy values were used to reconstruct a smoother power curve, enabling clearer comparisons between rotor configurations.

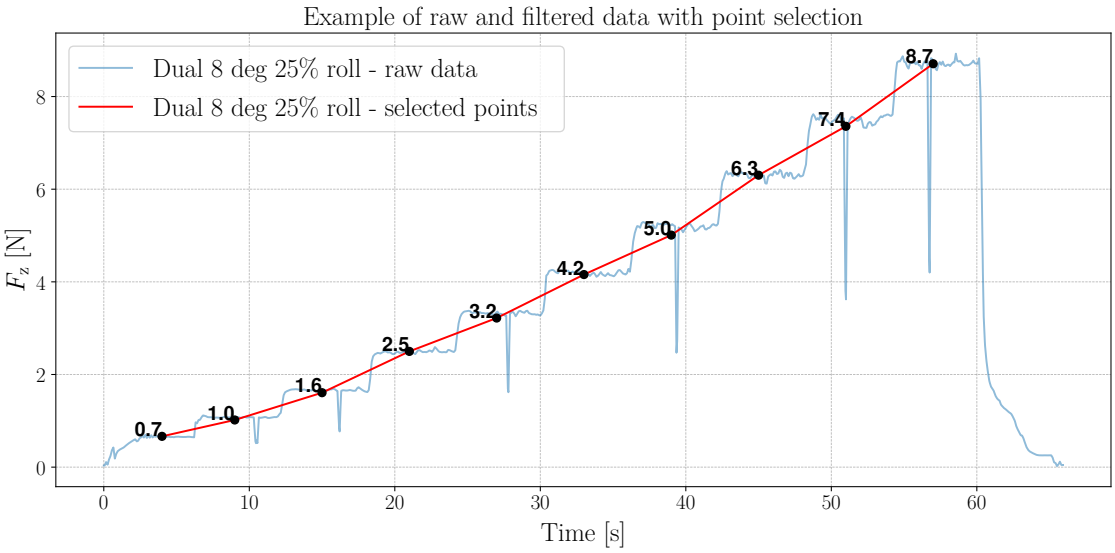

Figure 3.5: Raw data vs selected points.

4

Results

The results are presented in three sections. The first section covers the thrust and power consumption characteristics of the rotors under controlled testing conditions. The second section evaluates the dynamic response of each rotor through step response tests and visual analysis of blade motion. The third section provides qualitative observations on vibration characteristics observed during testing.

4.1 Thrust and power consumption

Thrust and power output were evaluated under two test conditions: (1) RPM sweep tests at fixed roll commands of, 25%, 50%, and 75%, and (2) roll sweep tests at constant RPM. These tests were conducted at three blade pitch angles of 8°, 10°, and 12° for both rotor types. The results provide insight into how thrust is distributed in the vertical and horizontal directions and how power demand varies with control inputs for each rotor.

4.1.1 RPM sweep at 25, 50 and 75% roll command

This section presents the results of the RPM sweep tests for all blade angles.

8 degree

Fig. 4.1 presents thrust and power results from the rpm sweep at an 8° blade angle. The Fig. displays measurements across RPM for both rotors.

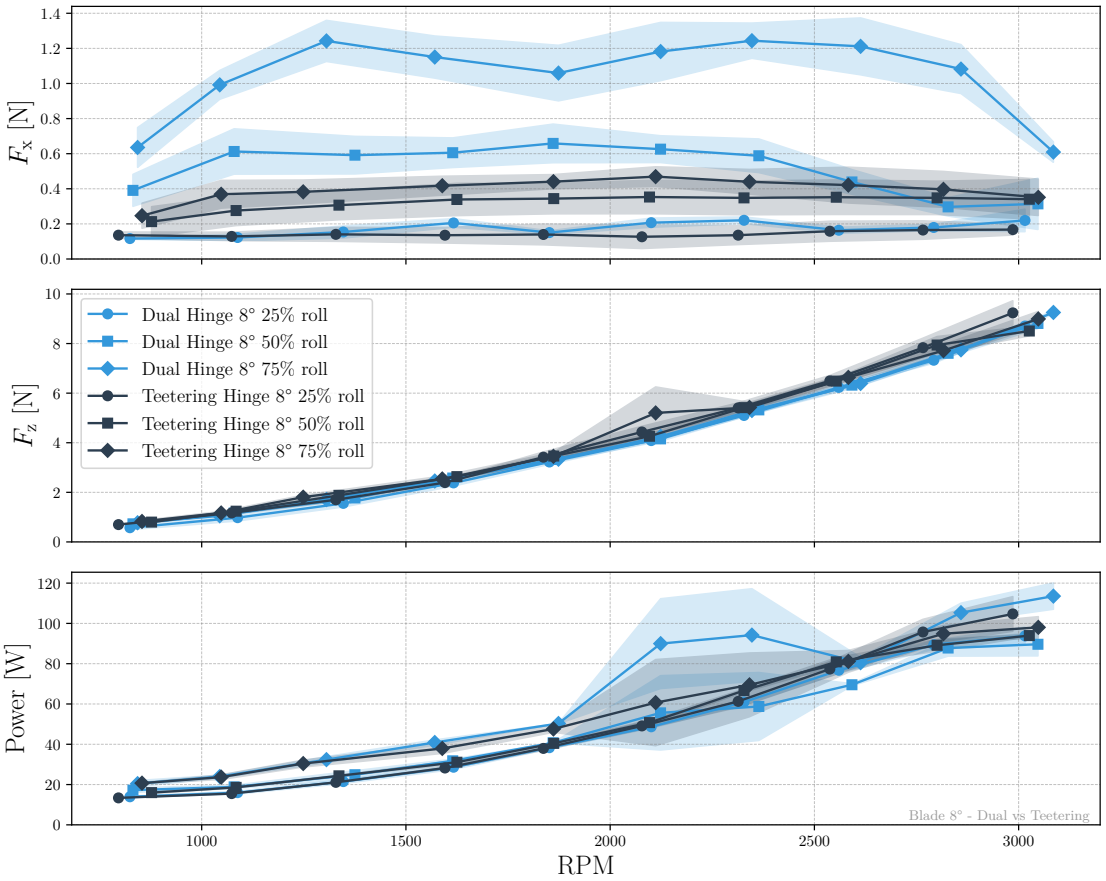

Figure 4.1: RPM sweep comparison at 8° blade angle.

10 degree

Fig. 4.2 presents thrust and power results from the rpm sweep at an 10° blade angle. The Fig. displays measurements across RPM for both rotors.

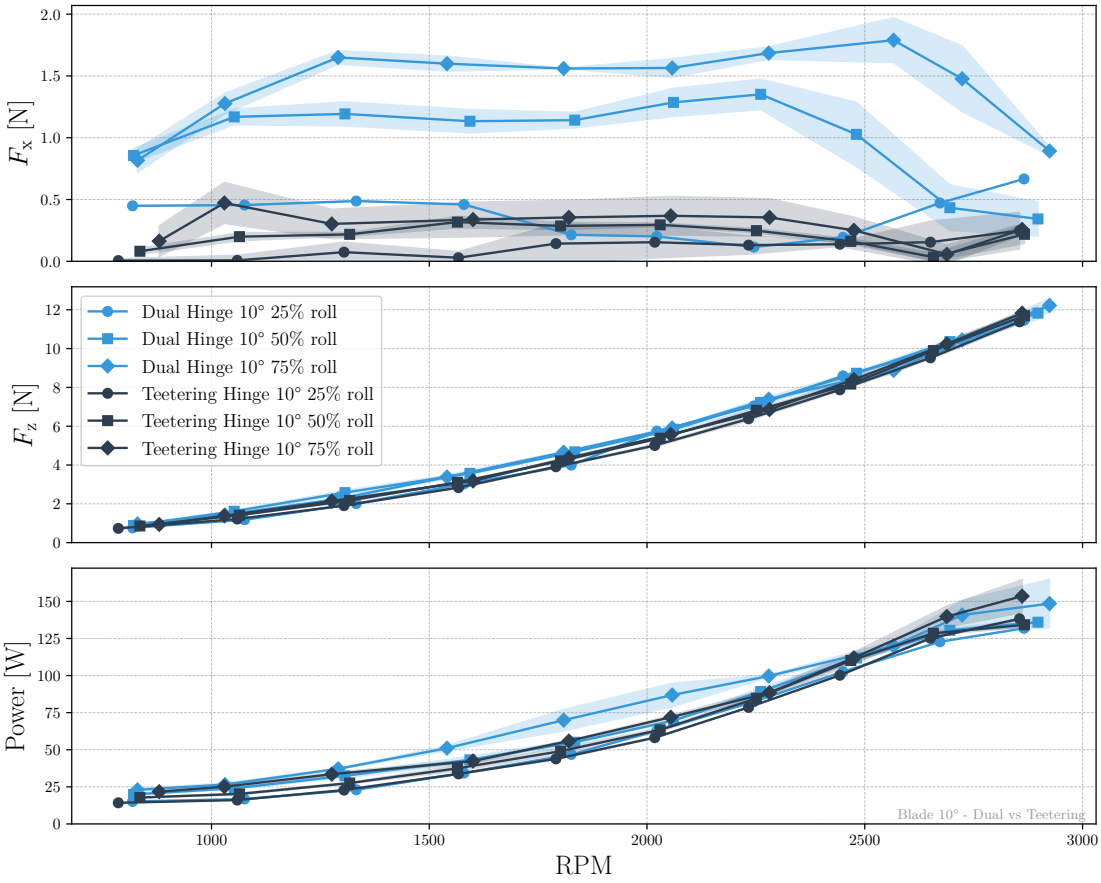

Figure 4.2: RPM sweep comparison at 10° blade angle.

12 degree

Fig. 4.3 presents thrust and power results from the rpm sweep at an 12° blade angle. The Fig. displays measurements across RPM for both rotors.

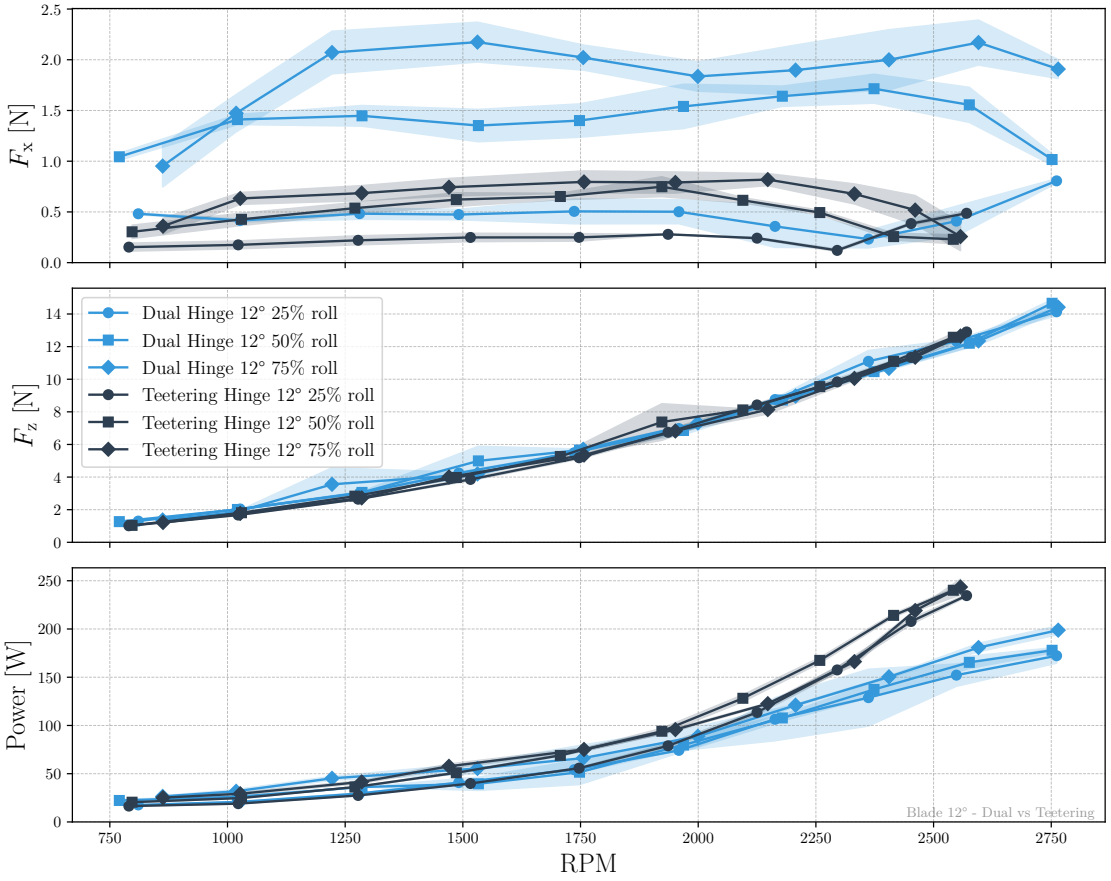

Figure 4.3: RPM sweep comparison at 12° blade angle.

4.1.2 Roll sweep at 1900 RPM

This section presents the results of the roll sweep tests for all blade angles.

8 degree

Fig. 4.4 presents thrust and power results from the roll sweep at an 8° blade angle. The Fig. displays measurements across roll commands for both rotors.

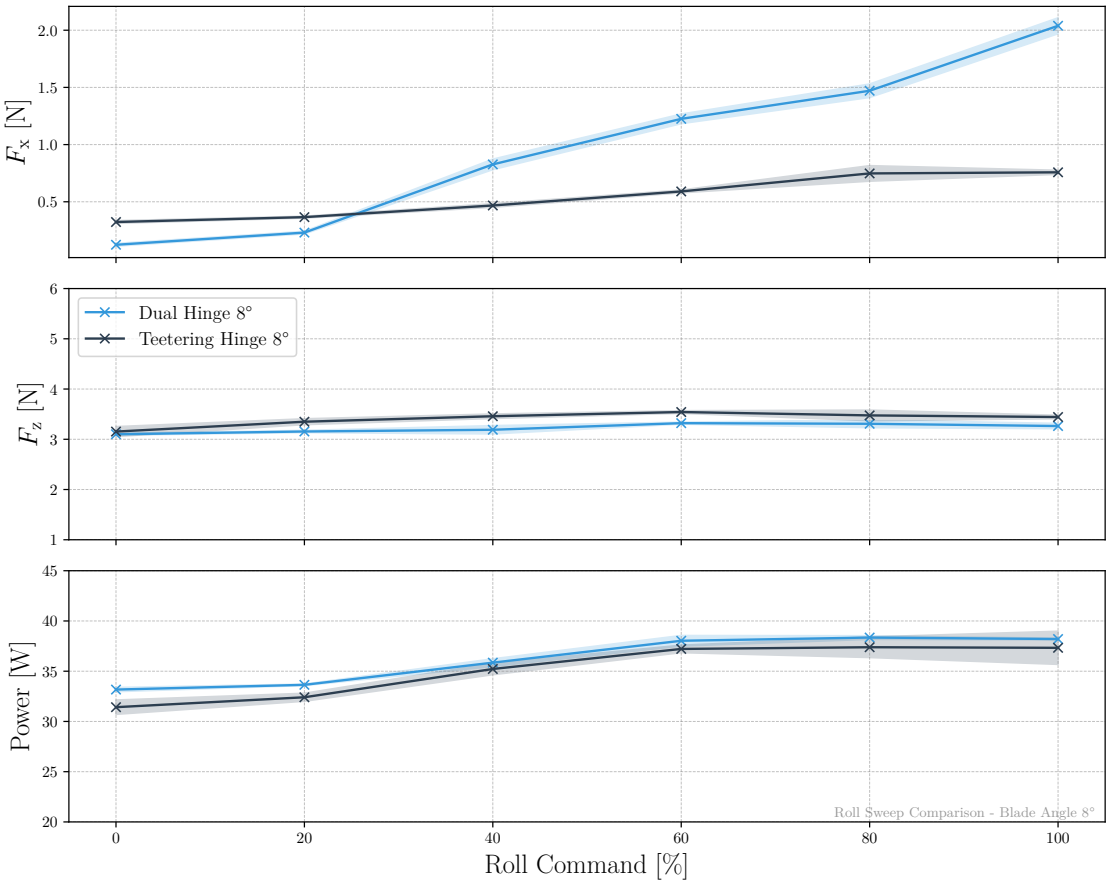

Figure 4.4: Roll sweep comparison at 8° blade angle.

10 degree

Fig. 4.5 presents thrust and power results from the roll sweep at an 10° blade angle. The Fig. displays measurements across roll commands for both rotors.

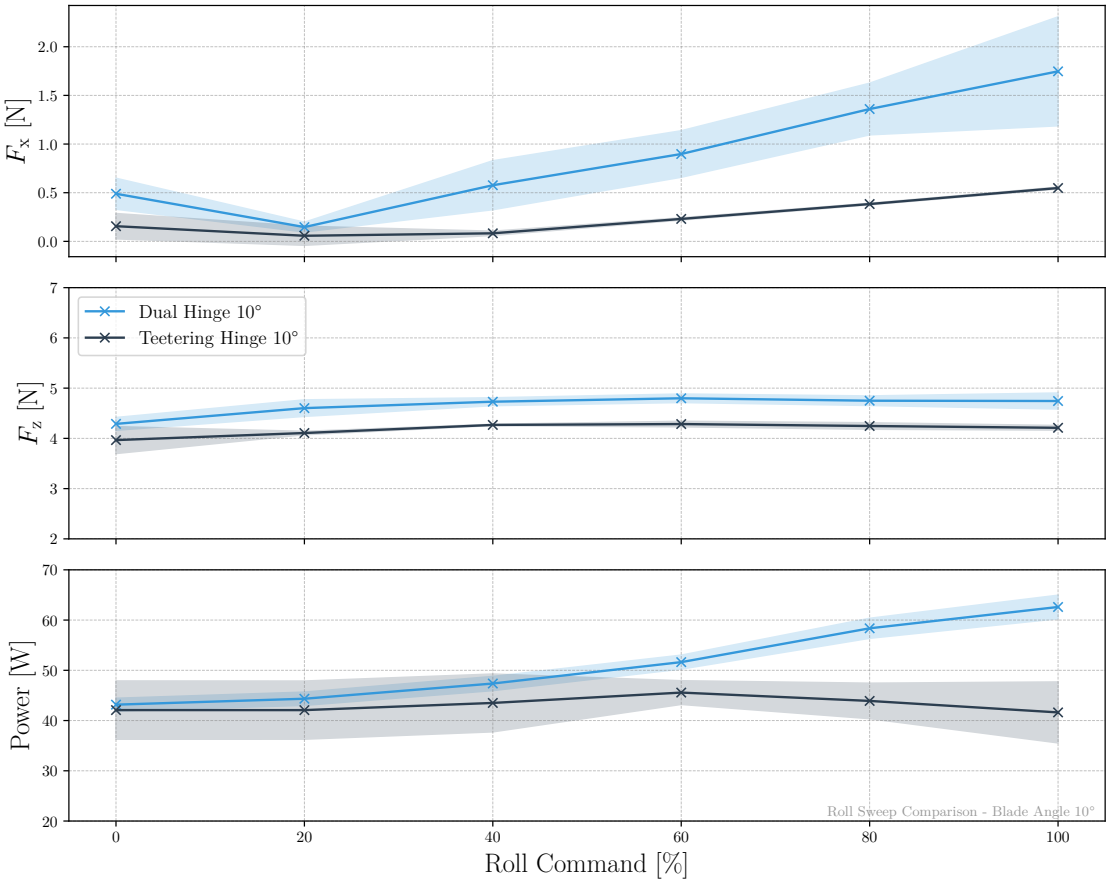

Figure 4.5: Roll sweep comparison at 10° blade angle.

12 degree

Fig. 4.6 presents thrust and power results from the roll sweep at an 12° blade angle. The Fig. displays measurements across roll commands for both rotors.

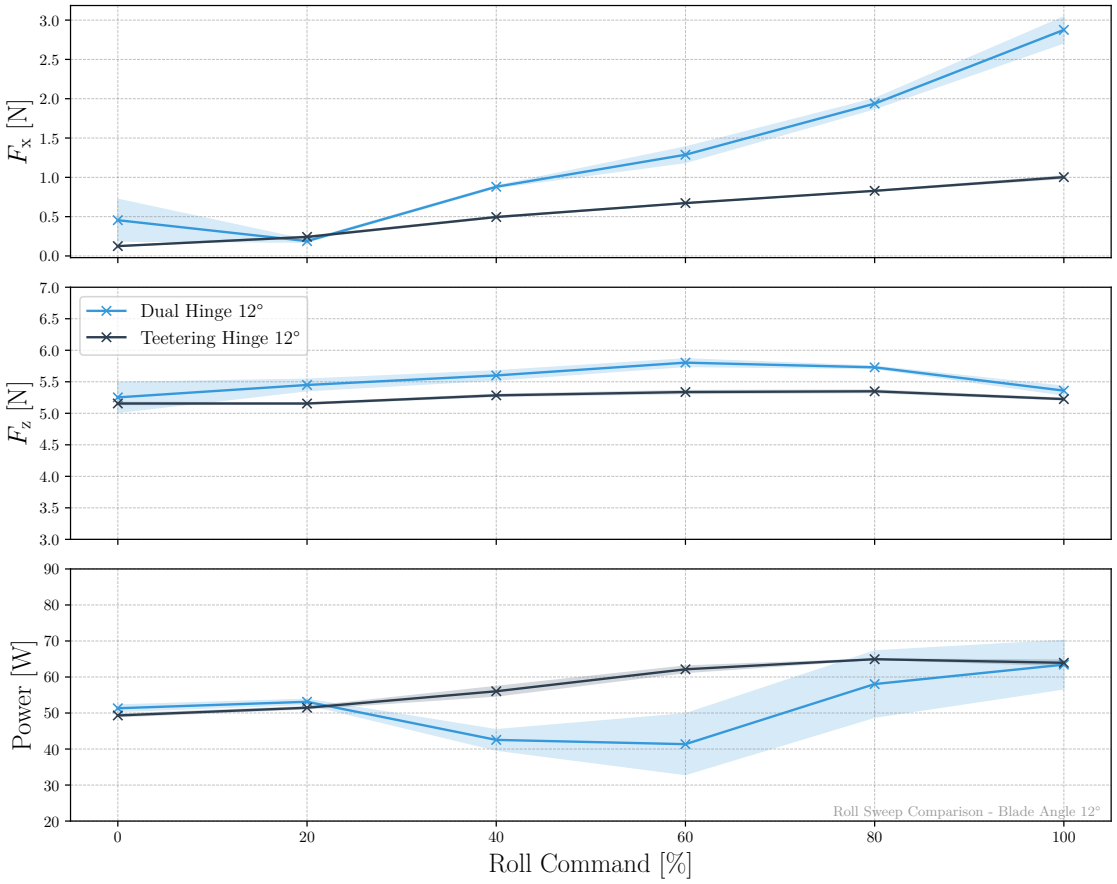

Figure 4.6: Roll sweep comparison at 12° blade angle.

4.1.3 Rotor response time

The step response of the rotor head illustrates the response time of the system giving an idea of the stability and manoeuvrability. The response time is measured using the methodology for the transient step response measurement resulting in a rise time measurement, shown in Figs. 4.7, 4.8 and 4.9.

Slow motion footage was captured using a 1500 frames per second camera to show the kinematics of the propeller blades, rotor hub and motor. The motor is rotating at a constant rate except for the modulation on top and the vectoring command is fixed.

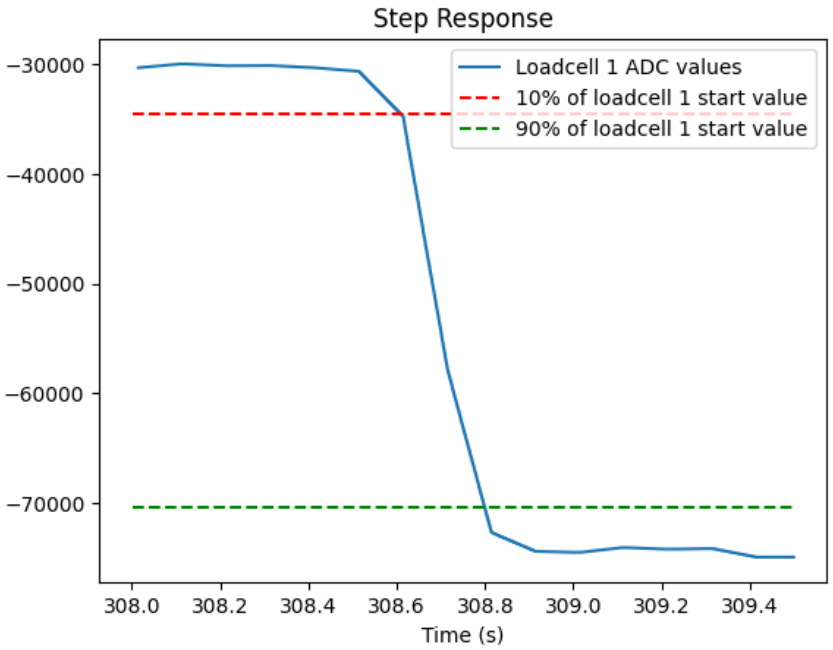

Figure 4.7: Transient step response for 10 deg AoA dual hinged rotor.

Table 4.1: Transient step response results

Rise time (s)	Run 1	Run 2
10° dual hinge	0.19	0.23
12° dual hinge	0.21	0.53
12° teetering hinge	0.17	0.22

4.1.4 Vibration

The teetering hinge rotor appeared to produce significantly more vibration during testing, although no quantitative measurement was made. A clear ghosting image was seen on the single teetering configuration indicating a oscillation not related to the modulation and substantial increase in sound during this.

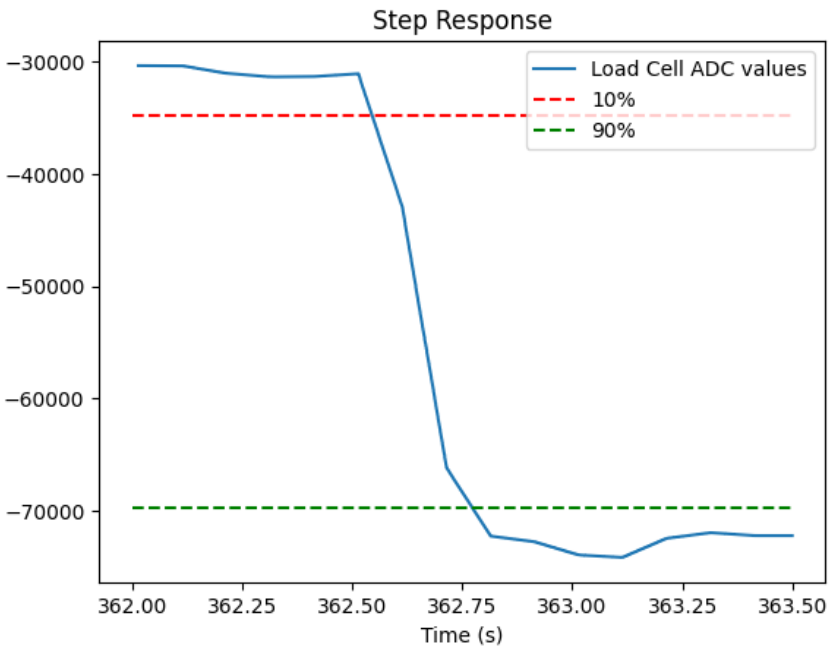

Figure 4.8: Transient step response for 12 deg AoA dual hinge rotor.

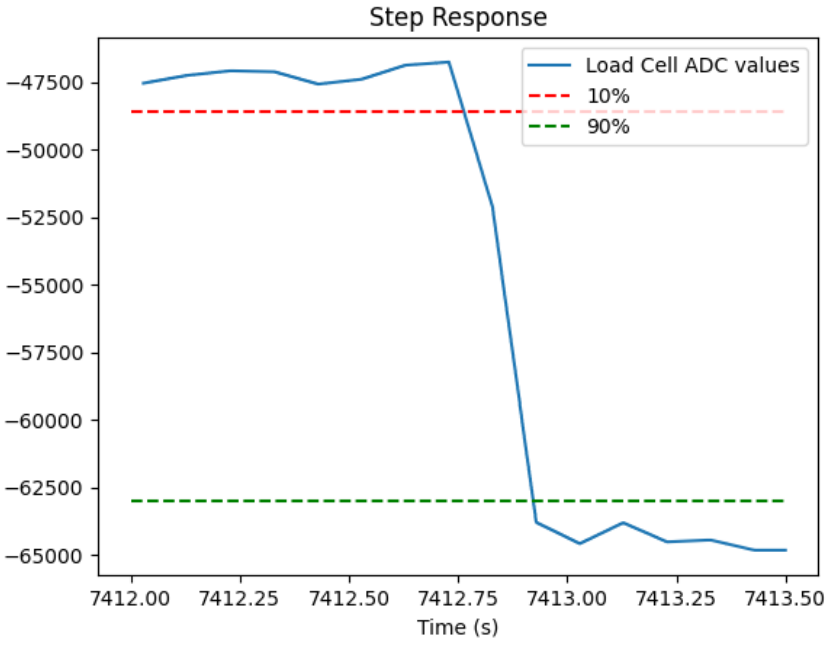

Figure 4.9: Transient step response for 12 deg AoA teetering hinge rotor.

(a) Zero acceleration. Maximum vectoring reached.

(b) Accelerating. Blades pitching increasing AoA. Jerk is positive.

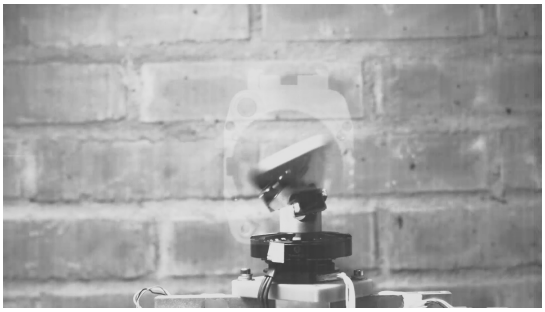

(c) Peak acceleration reached. Maximum cyclic lift generated. Jerk is zero.

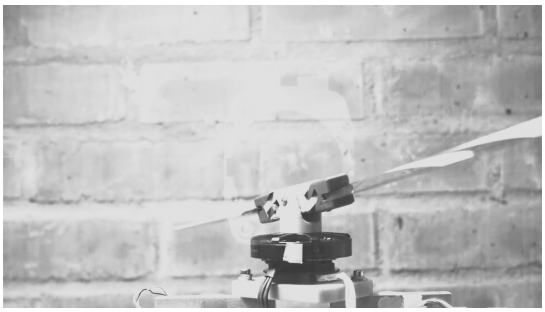

(d) Jerk negative. Max vectoring almost reached.

Figure 4.10: Single hinge rotor head vectoring and generating cyclic lift.

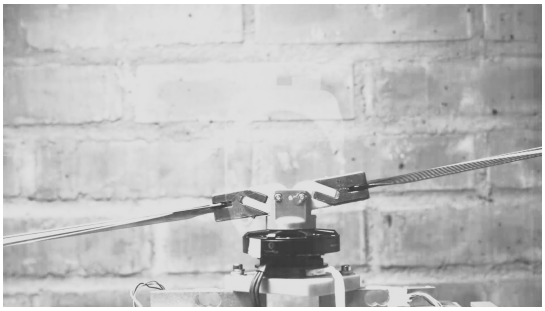

(a) Zero acceleration. Maximum vectoring reached.

(b) Accelerating. Blades pitching increasing AoA. Jerk is positive.

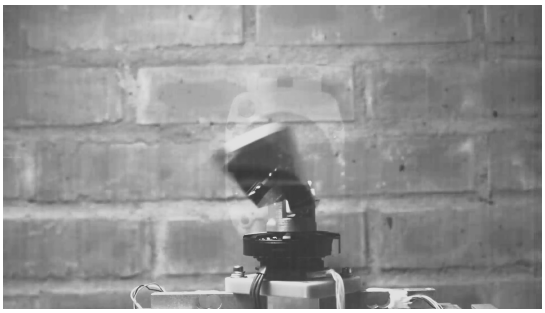

(c) Peak acceleration reached. Maximum cyclic lift generated. Jerk is zero.

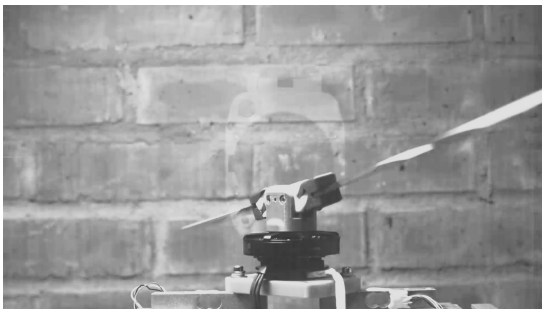

(d) Jerk negative. Max vectoring almost reached.

Figure 4.11: Dual hinge rotor head vectoring and generating cyclic lift.

5
Discussion

This chapter summarises the results obtained, highlighting key differences in performance and design characteristics between the two rotor configurations.

5.1 Thrust performance

The thrust measurements obtained from both the RPM and roll command sweeps provide insight into how each rotor responds to varying control inputs. As expected, thrust in both the vertical (Z) and horizontal (X) directions increases with rotor speed. However, the rate of change is influenced by both the blade angle and the rotor configuration.

Across all tests, the dual hinge rotor consistently produced significantly more horizontal thrust, typically 2 to 3 times higher than that of the teetering hinge rotor. This was true across all blade angles (8°, 10°, and 12°) and roll commands, as illustrated in Figs. 4.1 through 4.3. In contrast, the vertical thrust remained nearly identical between the two rotors, which was expected since both used the same blades and operated at matched RPMs and blade angles. Due to the higher horizontal thrust generated by the dual hinged rotor an aircraft equipped with this design should be able to accelerate faster in the horizontal direction and being able counteract any movement increasing manoeuvrability and stability in the affected directions. Horizontal manoeuvrability and stability is key when carrying sensors and therefore the dual hinged version is the superior version for RQ1.

In the roll sweep tests, both rotors exhibited increased horizontal thrust with higher roll input, with the dual hinge again showing superior performance. Vertical thrust stayed approximately constant throughout the sweep, indicating that roll control did not significantly affect lift.

Power consumption trends were generally consistent and matched expectations at 8° AoA (Fig. 4.4). However, deviations were observed at higher angles. At 10° (Fig. 4.5), the dual hinge rotor showed increased power consumption from around 60% roll command onwards. At 12° (Fig. 4.6), it displayed an unexpected dip in power between 20% and 60% roll input, returning to similar values as the teetering rotor by 100% roll command. The power consumption is somewhat inconsistent in the data, but the trend does show the teetering rotor head consuming more power and generating less horizontal thrust overall reducing its performance in terms of RQ2.

These anomalies may be due to aerodynamic effects such as local blade stall, complex turbulent interactions, or simply undersampled data. High-speed video was recorded, but no visible mechanical issues or structural problems were observed in either rotor during these tests.

5.2 Design impacts and mechanical performance

The differences in construction between the teetering and dual hinge rotors are clearly reflected in their dynamic behaviour. The dual hinge rotor allows each blade to flap independently, unlike the teetering hinge where both blades are mechanically linked. As a result, the dual hinge rotor achieves slightly larger flapping angles, which appears to be a key factor contributing to its ability to generate higher horizontal thrust.

Due to undersampling in the power measurements, only general trends can be interpreted with confidence. Across most RPM sweep tests, power consumption was comparable between the two rotor types. However, a notable deviation occurs at the 12° blade AoA, as shown in Fig. 4.3, where the teetering hinge rotor consumes approximately 45 percent more power at maximum RPM.

While the precise rotor dynamics at high RPM remain uncertain, a likely explanation is that the teetering rotor experiences greater aerodynamic drag and especially at higher blade angles. These effects could increase the torque demand on the motor during acceleration, which in turn leads to higher overall power consumption for the teetering rotor in this RPM range. However, the discrepancy could also be a result of the previously mentioned undersampled power measurements. Without additional testing at this RPM range using improved measurement equipment, it is difficult to determine the cause with certainty.

Worth noting during all runs when increasing the RPM and doing any meaningful amount of roll command the teetering rotor head generated substantially more audible noise and creating large amounts of vibrations in the frame. This could have generated by any type of resonance of the test setup but since this was apparent at all higher RPMs resonance is an unlikely candidate since it should be apparent at specific frequencies. This is more likely an systemic flaw in the constrained nature of the teetering design which causes these sounds and vibrations. This would also explain the increased power consumption at theses states. When optimizing these designs for future work it would be important to take into account these vibrations to avoid any catastrophic disintegrations from fatigue in the material.

5.3 Response time and stability analysis

Analysis of the step response data in Table 4.1 and review of high speed camera footage revealed no significant difference in rotor response time between the two

configurations. Although no vibration sensor was included in the test rig, the teetering rotor clearly exhibited substantially higher vibration levels than the dual hinge. This caused the configuration to produce substantially more sound than the dual hinged version. This was expected, given the teetering hinge's inherently more rigid design, which forces the blades to bend under load rather than flap independently as in the dual hinge rotor. No significant difference in stability was observed from the high speed footage. Both rotors operated smoothly and appeared stable during one revolution of the rotor head.

5.4 Design trade-offs and application suitability

One of the main objectives of this thesis was to explore the suitability of these rotors for use in sensor carrying drones. Without flight testing it is still difficult to say with full confidence which design is more suitable overall. However, based on the results obtained, the dual hinge shows a clear advantage in terms of reduced vibrations and considerably better thrust vectoring capabilities.

Since both rotors have shown strong performance and work well with the control system developed, they both have potential. Further development into flying drones would be beneficial for more conclusive testing. Continued refinement of each design could also reveal additional strengths or weaknesses not visible in the test setup.

6
Conclusion

This thesis set out to investigate two conventional helicopter rotor types, evaluating their suitability for swashplateless rotor systems and their potential for use in sensor carrying drone applications. It also aimed to advance these systems through mechanical design improvements and control software development.

Under identical operating conditions, the dual hinge rotor consistently outperformed the teetering rotor in terms of horizontal thrust, matched its vertical thrust performance and generated significantly lower vibrations while maintaining comparable power consumption. By increasing the AoA of the blades there was a significant increase in thrust in both cases, but the dual hinged rotor continued to dominate at all AoA variants. Despite the large difference in thrust generated no difference in the dynamic response was measured and therefore both rotor heads responded equally fast to a control input.

These differences are closely linked to the underlying mechanical designs. The dual hinge rotor's independent blade flapping allows for more effective force generation, which contributes to both better thrust performance and reduced vibrations in the rotor head. This is particularly valuable in sensor carrying drones, where stability and precision are critical.

Overall, this work demonstrates that swashplateless rotor systems are not only viable but may offer real advantages in UAV applications for reducing the bill of material of an aircraft and possibly increasing the effectiveness. By utilizing the high performance of today's modern flight controllers and motor control hardware allows modern UAVs to solve old mechanical problems in old school aircrafts and transform it into a pure electrical and software solution. In this case the dual hinge rotor in particular shows strong promise for the application, but both configurations deserve further exploration through flight testing.

Future Work

Although both rotor configurations performed almost flawlessly and exceeded expectations in terms of control, the test rig used for evaluation revealed several limitations. The original load cell setup (arranged in a T formation) experienced severe vibrations and had to be redesigned. In the revised setup, the load cells were mounted horizontally for added stiffness. Even so, the RPM and roll inputs had

to be limited to avoid resonance issues, one of which caused damage to a load cell during testing. Lowering the RPM and roll inputs also forced the load cells to operate far from their ideal measuring range. A more suitable setup would involve using a six-axis load cell, which would provide greater reliability and capture rotor performance in finer detail over a wider operating range.

Power measurement posed similar challenges. Since batteries were used, they had to be recharged frequently to keep conditions consistent. This added variability and limited test stability. A more effective approach would be to use a power supply capable of handling the dynamic BEMF (Back- Electric magnetic field) generated by the motor when accelerating and de-accelerating. It could also allow for a better estimation power consumed by measuring at a higher rate.

While the static tests provided valuable insights, they do not replicate the dynamics of real flight. Therefore a proper airframe utilizing both rotor types would provide valuable information. This airframe should be able to mimic an equivalent conventional helicopter demonstrating the effectiveness and usability of the proposed rotor types explored in this thesis. This demonstrator could mimic a single-rotor helicopter with a tail rotor or a tandem helicopter utilizing two swashplate-less rotor heads.

By increasing the scope one should compare the helicopter airframe with either rotor types with an arguably functionally equivalent multicopter. This multicopter should be similar in terms of the size and weight. This could show the effectiveness of using a single large rotor for thrust and control compared to multiple small rotors utilized by a multicopter.

Furthermore, applying the same control parameters to both rotors may have limited their individual potential. Therefore, investigating and normalizing the control parameters for each rotor could allow for a fairer comparison in the case that there was a difference in the preferred range for the control parameters. Future work should therefore include rotor-specific control tuning and flight testing to better understand real-world performance. An upgraded test rig with better aerodynamic properties and reduction of any ground effects or wind tunnel effect created by the safety barrier. This would ideally be combined with a six-axis load cell with a suitable bi-directional power supply with high speed power measurement, would significantly improve data quality and reliability.

Bibliography

[1] Paulos, J., & Yim, M. (2013). *An underactuated propeller for attitude control in micro air vehicles.* In *2013 IEEE/RSJ International Conference on Intelligent Robots and Systems* (pp. 1374-1379). IEEE. doi:10.1109/IROS.2013.6696528

[2] Paulos, J., & Yim, M. (2017). *Cyclic Blade Pitch Control Without a Swashplate for Small Helicopters* In *Journal of Guidance, Control and Dynamics* DOI: 10.2514/1.G002683

[3] Paulos, J., Caraher, B, & Yim, M. (2017). *Emulating a Fully Actuated Aerial Vehicle using Two Actuators* In *2018 IEEE International Conference on Robotics and Automation (ICRA)* (7011-7016) IEEE. DOI: 10.1109/ICRA.2018.8462975

[4] PX4 Development Team (2025),. *Helicopters - PX4 User Guide* 2025. [Online]. Available: `https://docs.px4.io/main/en/frames_helicopter/`. [Accessed: 14-Mar-2025].

[5] PX4 Development Team (2025). *Controller Diagrams - PX4 User Guide* 2025. [Online] Available: `https://docs.px4.io/main/en/flight_stack/controller_diagrams.html` [Accessed: 14-May-2025]

[6] L. J. Clancy (1978) *Aerodynamics* Available: `https://archive.org/details/aerodynamics0000clan` [Accessed: 14-May-2025]

[7] Group Captain A. Fanklin RAF (2020) AP3456 The Central Flying School (CFS) Manual of Flying Available: `https://assets.publishing.service.gov.uk/government/uploads/system/uploads/attachment_data/file/857310/Volume_12_Helicopters.pdf`

[8] Cadence CFD *Exploring the Aerodynamics of Symmetrical Airfoil* Available: `https://resources.system-analysis.cadence.com/blog/msa2022-exploring-the-aerodynamics-of-symmetrical-airfoil` [Accessed: 14-May-2025]

[9] M. Hepperle (2018) *Aerodynamic Characteristics of Propellers* Available: `https://www.mh-aerotools.de/airfoils/propuls3.htm`

[10] Flores, J., Salazar, S., Gonzalez-Hernandez, I., Rosales, Y., Lozano, R., Salazar, E., and Nicolas, B. (2024). Control of Helicopter Using Virtual Swashplate. *Drones*, **8**(7), 327. `https://doi.org/10.3390/drones8070327`

[11] Tom Stanton, “How I built a Swashplateless Helicopter”, *YouTube*, Sep. 2021. [Online]. Available: `https://youtu.be/Y31BhQToh_U` [Accessed: May 21, 2025].

[12] Davide Faconti, “PlotJuggler (3.10)“, *Github*, April 2025 [Online] Available: `https://plotjuggler.io/` [Accessed: April 30, 2025]

DEPARTMENT OF MECHANICS AND MARITIME SCIENCES
CHALMERS UNIVERSITY OF TECHNOLOGY
Gothenburg, Sweden 2025
www.chalmers.se

CHALMERS
UNIVERSITY OF TECHNOLOGY